

## Experimental determination of the Landau Fermi-liquid-theory parameters: Spin waves in rubidium

Daniel Pinkel\* and Sheldon Schultz

University of California at San Diego, La Jolla, California 92093

(Received 4 April 1977)

This paper presents the results of a study made on spin waves in high-purity rubidium foils at cryogenic temperatures ( $\approx 1.4$  K). The measurements were made using the microwave-transmission technique at  $X$ -band microwave frequencies and represent an extension of previous measurements in sodium and potassium. From a comparison of the data with theoretical line-shape formulas based on the Landau Fermi-liquid theory, we deduce values of the first three Legendre coefficients of the spin-dependent part of the Landau interaction function. The values are  $B_0 = -0.21 \pm 0.05$ ,  $B_1 = +0.03 \pm 0.08$ , and  $B_2 = -0.09 \pm 0.1$ . The errors are not independent, and the consequent relationships between the coefficients consistent with our measurements are presented in detail. A discussion of the particular experimental difficulties encountered and their implications for the analysis is given. We include an analysis of a simple model that exhibits the essential features of spin-wave behavior in itinerant interacting electron systems.

### I. INTRODUCTION

In this paper we present the extension of precision conduction-electron spin-wave measurements to a third metal, rubidium. We have previously presented measurements in Na and K (henceforth I).<sup>1</sup> From our measurements we can deduce values for the Landau Fermi-liquid parameters  $B_0$ ,  $B_1$ , and  $B_2$ . These parameters describe the effective many-body interactions between the conduction electrons. The spin waves are observed by studying the transmission of microwave power through thin ( $\approx 0.2$  mm) foils of metal as a function of magnetic field at cryogenic temperatures. Peaks in the transmitted field occur whenever a standing-spin-wave mode is excited in the sample. These peaks appear split off from the normal  $g \approx 2$  conduction-electron spin-resonance (CESR) signal that exists even in the limit of zero interactions. In Fig. 1 we present a typical signal seen in Rb. The spin-wave excitations do not exist in a non-interacting electron gas, and are the only experimentally observed signals known to us to depend completely on the existence of many-body interactions. From measurements on the observed spin waves, we can determine the character of the many-body interactions.

The paper is organized in the following way. In Sec. II we discuss the basis of spin-wave theory, including an analytic investigation of predicted spin-wave behavior. Section III describes the experimental techniques and apparatus used in this work. Section IV discusses the data obtained, including the rather complicated method that had to be used for determining the thickness of the samples. In Sec. V we present the data analysis. Section VI compares these measurements with other

work and discusses possible directions for future research. The Appendix contains an analysis of a simple, classical, one-dimensional model of an interacting electron gas that facilitates the visualization of the spin dynamics in a spin wave.

### II. THEORY

As a more complete outline of the Landau theory is presented in I, it will not be repeated. We present a very brief review to lay the groundwork for the rest of the discussion.

In 1956 Landau<sup>2</sup> proposed a phenomenological theory to describe the low energy excitations of interacting Fermi systems. This approach has since been shown to be exact within the framework of perturbation theory. Later, Silin<sup>3</sup> extended the theory to charged systems by taking account of the long-range Coulomb interactions via Poisson's equation and the macroscopic charge density. The books by Pines and Nozières<sup>4</sup> and Platzman and Wolff<sup>5</sup> contain good discussions of the theory.

In the Landau Fermi-liquid theory, the interactions between a particle of momentum  $\vec{p}$  and spin  $\sigma$  and another of momentum  $\vec{p}'$  and spin  $\sigma'$  are described by an interaction function  $f(\vec{p}, \sigma; \vec{p}' \sigma')$ . If the system is not magnetic, has a plane of reflection symmetry, and lacks spin-orbit coupling, the interaction function can be written as the sum of two parts, one spin independent and the other spin dependent.

$$f(\vec{p}, \sigma; \vec{p}', \sigma') = A(\vec{p}, \vec{p}') + B(\vec{p}, \vec{p}') \vec{\sigma} \cdot \vec{\sigma}'. \quad (1)$$

If the Fermi surface is spherical and only low-energy excitations are considered, the magnitudes of  $\vec{p}$  and  $\vec{p}'$  are both equal to the Fermi momentum  $p_F$ .  $A$  and  $B$  are independent of the interchange of

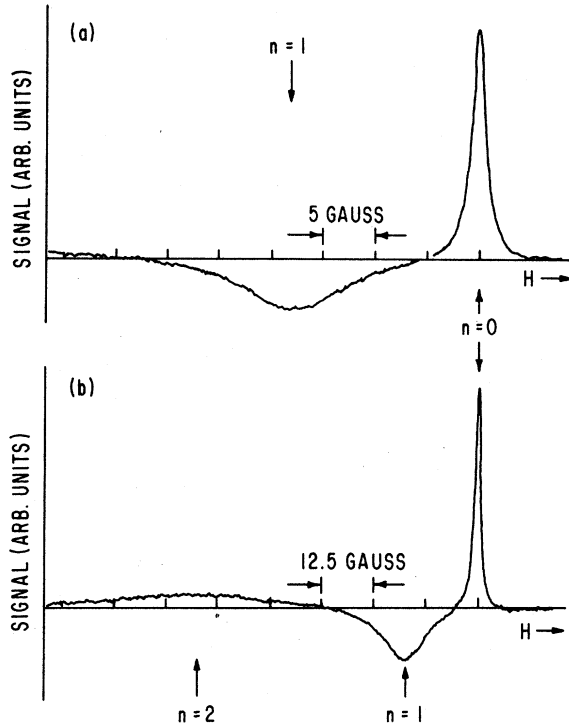


FIG. 1. Transmitted microwave field vs dc magnetic field at  $\Delta=90^\circ$  in sample Rb-7.  $L=0.17 \pm 0.0025$  mm,  $\nu=9.1955$  GHz,  $T=1.4$  K. (a) A sweep through the CESR ( $n=0$ ) and first spin wave ( $n=1$ ). (b) The sweep has been expanded, at the same gain, to include the second spin wave ( $n=2$ ).

$\vec{p}$  and  $\vec{p}'$  so the only functional dependence is on the angle between them. Thus  $A$  and  $B$  can be expanded as a series of Legendre polynomials. Including normalization factors, the expansions are written

$$A(\vec{p}, \vec{p}') = \frac{1}{\nu_0} \sum_{n=0}^{\infty} A_n(2n+1) P_n(\cos\theta), \quad (2)$$

$$B(\vec{p}, \vec{p}') = \frac{1}{\nu_0} \sum_{n=0}^{\infty} B_n(2n+1) P_n(\cos\theta),$$

where  $\nu_0$  is the density of states at the Fermi surface. It is the presence of nonzero parameters  $B_n$  that lead to spin waves in the conduction electrons of metals and the interpretation of the spin-wave spectra allows the measurement of the  $B_n$ 's.

Rubidium does not come as close as sodium and potassium to meeting the restrictions leading to Eq. (2). From de Haas-van Alphen (dHvA) studies<sup>6</sup> there is known to be a 1.5% nonsphericity in the Fermi surface. For Na and K this is less than 0.2%. The spin-orbit coupling is also expected to be stronger than in Na and K. These points will become important in light of the experimental results.

Platzman and Wolff<sup>7</sup> (PW) have worked out the spin-wave theory to order  $q^2$ . To this order only  $B_0$  and  $B_1$  enter. Their results give an excellent description of the observed spin-wave behavior and are more or less analytically tractable and will be discussed briefly below. Wilson and Fredkin (WF) have developed the theory to all orders in  $q^2$  and for an arbitrary number of  $B_n$ 's. It is with their more exact results that the data was compared to extract the values for the Landau parameters. Because of its complexity we will not discuss the WF theory further. Interested readers are referred to Ref. 8. The Appendix contains a simple classical model that allows visualization of the self-consistent spin motion that occurs in a spin wave.

PW found that to order  $q^2$  the dispersion relation is given by

$$q^2 = \frac{\omega_0 - \omega - i/T_2}{iD^*}, \quad (3)$$

$$D^* = \frac{1}{3} v_F^2 \tau (1+B_0)(1+B_1)(1+iX_1\omega_0\tau) \times \left( \frac{\cos^2\Delta}{(1+iX_1\omega_0\tau)^2} + \frac{\sin^2\Delta}{\omega_c^2\tau^2(1+B_1)^2 + (1+iX_1\omega_0\tau)^2} \right).$$

Here  $T_2$  is the spin relaxation time,  $\tau$  is the momentum collision time,  $\Delta$  is the angle between the magnetic field and  $q$ ,  $\omega_c$  is the cyclotron frequency  $eH/m^*c$ ,  $m^*$  is the effective mass,  $\omega_0 = g\mu_B H/\hbar$ , and  $X_1 = (B_1 - B_0)/(1+B_0)$ .

A feeling for the general behavior of the spin-wave mode can be obtained by looking at graphs of the dispersion relation. Figure 2 shows graphs of  $\text{Im}(q)$  vs  $\text{Re}(q)$  for three particular  $\Delta$ 's, with values of the other parameters appropriate for the alkali metals. Progress along the curves is parametrized by  $\omega \sim \omega_0$ . Part (a) shows the case when  $\Delta=0^\circ$  and the wave is propagating parallel to the applied magnetic field. The wave will propagate only when  $\text{Im}(q)$  is small, which requires  $\omega_0 > \omega$  at this angle. The dispersion relation asymptotically approaches the two orthogonal dotted lines for large  $|\omega - \omega_0|$ . It reduces to these lines as the spin relaxation time  $T_2$  becomes infinite. The angle  $\alpha/2$  depends on  $\tau$  and for small angles is  $1/2X_1\omega_0\tau$ . Thus, damping due to  $T_2$  is dominant only near  $\omega = \omega_0$ . As the transmission of microwave power through a finite slab of metal will be enhanced whenever a standing spin wave exists, we expect transmission peaks at  $\text{Re}(q) = n\pi/L$ , where  $L$  is the sample thickness. For samples in which the CESR and spin waves are well resolved, the first spin wave occurs at a value of  $\text{Re}(q)$  for which the damping is dominated by  $\tau$ . A more standard presentation of the dispersion relation, valid for infinite  $\tau$  and  $T_2$ , is shown in

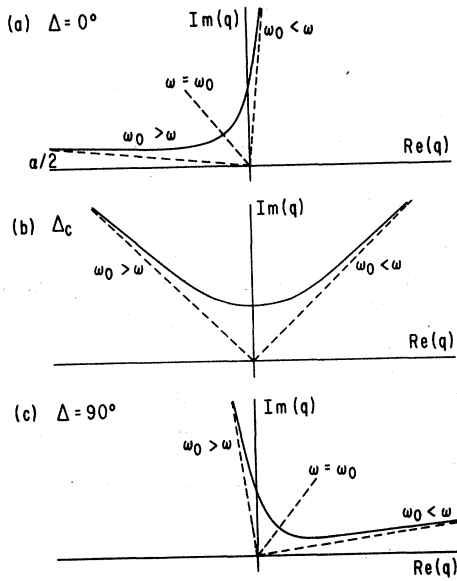


FIG. 2. Graph of the real and imaginary parts of  $q$  from the PW dispersion relation at fixed magnetic field. The curves are parametrized by  $\omega - \omega_0$ . (a)  $\Delta = 0^\circ$ , magnetic field perpendicular to the sample; (b)  $\Delta = \Delta_c$ , the spin wave critical angle; (c)  $\Delta = 90^\circ$ , magnetic field parallel to the surface. The spin-wave mode propagates where  $\text{Im}(q)$  is small. The peaks occur near  $\text{Re}(q) = n\pi/L$ .

Fig. 3. The points where transmission peaks occur are marked.

As  $\Delta$  is changed (by rotating the magnetic field) the curvature of the dispersion relation in Fig. 3 is reduced, and the position of the spin-wave peaks move closer to the CESR peak at  $\omega = \omega_0$ . This shift is fundamentally due to the fact that the cyclotron motion of the electrons is becoming important. This same change is reflected in Fig. 2(a) primarily by a change in scale of the  $\text{Re}(q)$  and  $\text{Im}(q)$  axes. In the alkali metals the values of the parameters  $B_0$ ,  $B_1$ ,  $m^*$ , etc. are such that there exists an angle, called the critical angle  $\Delta_c$ , where the infinite  $\tau$  and  $T_2$  dispersion curve is flat (to order  $q^2$ ), as illustrated in Fig. 3. The same situation is alternatively shown in Fig. 2(b) for finite  $\tau$  and  $T_2$ . If  $X_1\omega_0\tau$  and  $\omega T_2 \gg 1$ , the rotation from 2(a) to 2(b) takes place over a small angular region near  $\Delta_c$ . At  $\Delta_c$  the transmitted signal is essentially symmetric, consisting of a main peak and perhaps some small negative lobes on either side.

As the magnetic field is rotated still farther to  $\Delta = 90^\circ$ , the dispersion relation is represented by the upper curve in Figs. 3 and 2(c). Now the spin-wave mode is weakly damped on the other side of  $\omega_0$ . The damping here is again proportional to  $1/\omega_0\tau$  but the factor is slightly different than at  $\Delta = 0^\circ$ . In summary, we expect to observe the

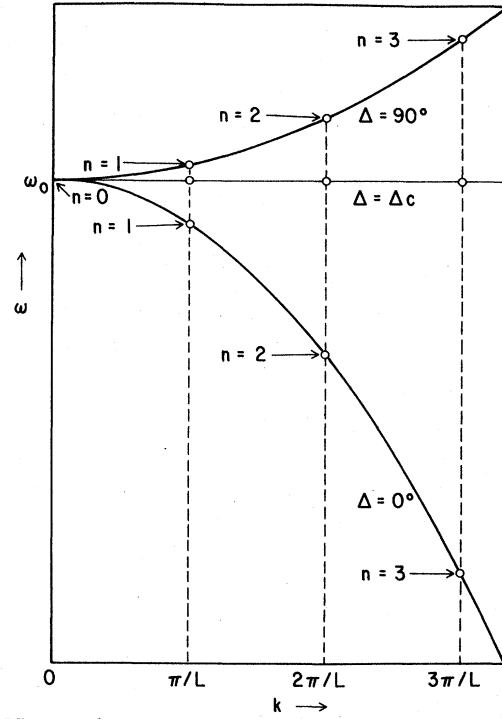


FIG. 3. Schematic spin-wave dispersion relation for conduction electrons at constant magnetic field. The relation is sketched for three values of  $\Delta$ :  $\Delta = 0^\circ$ ,  $\Delta_c$ , and  $\Delta = 90^\circ$ . The first four allowed wave vectors are shown. These satisfy the relation  $qL = n\pi$ , where  $L$  is the sample thickness.

spin waves at a higher magnetic field than the CESR when  $\Delta = 0^\circ$ . As the magnet is rotated, they move closer to the CESR and eventually at the critical angle they coalesce with it. As the magnetic field is rotated still farther, the spin waves appear on the low-field side.

In the limit of large  $X_1\omega_0\tau$  and large  $T_2$ , where the spin waves and CESR are well resolved, it can be shown that the spin waves are Lorentzian in shape and that the separation of the  $n$ th spin wave from the CESR is given by

$$\Delta\omega_n = \text{Re}(iD^*n^2\pi^2/L^2) \quad (4)$$

and its width by

$$\delta\omega_n = \text{Im}(iD^*n^2\pi^2/L^2). \quad (5)$$

Note that the spacing of the  $n$ th spin-wave peak from the CESR is proportional to  $n^2/L^2$ . In practical cases  $\delta\omega_n \propto 1/\tau$  there is a simple relation between the separation at an arbitrary angle  $\Delta$  and that at  $\Delta = 90^\circ$ .

$$\frac{\Delta\omega_n(\Delta)}{\Delta\omega_n(90^\circ)} = 1 - \left( \frac{2m(1+B_1)}{gm^*X_1} \right)^2 \cos^2\Delta, \quad (6)$$

where "g" is the electronic g value.

The critical angle occurs when  $\Delta\omega_n(\Delta_c) = 0$ . Thus

$$\cos^2 \Delta_c = [m^* g X_1 / 2m(1 + B_1)]^2. \quad (7)$$

In the framework of the PW calculation, the experimental determination of  $B_0$  and  $B_1$  requires the measurement of the first spin-wave spacing at two values of  $\Delta$ . Then supplying the other parameters from different sources allows solution for the two unknowns. Note that measuring more than one spin-wave peak at the same value of  $\Delta$  adds no new information since the same combination of  $B_0$  and  $B_1$  enter in determining the positions of all of them. The PW theory, however, is accurate only to order  $q^2$ . The WF calculation shows that to order  $q^4$  the parameter  $B_2$  enters, and that for each successive power of  $q^2$  in the expansion, another Landau parameter becomes important. For samples of the thickness (and thus  $q$  vectors) used in these experiments, the  $q^2$  expansion is adequate for describing the first spin-wave peak, as will be discussed later. Thus  $B_0$  and  $B_1$  can be determined by measuring the first spin-wave separation at two values of  $\Delta$ . With  $B_0$  and  $B_1$  known, measurement of the second spin-wave peak at some  $\Delta$  then allows the fitting of  $B_2$  assuming  $B_3$  and higher coefficients are not yet important (or are zero).

The two angles at which we have decided to make accurate measurements are  $\Delta_c$  and  $\Delta = 90^\circ$ . Background signals at other angles, such as that shown in Fig. 12, dictate this choice. In Na and K this baseline could be suppressed by going to thicker samples because the spin waves are attenuated less rapidly than the background signals. In Rb this could not be done because the signals we used for sample thickness determination (Sec. IV B 2) would also have been attenuated. At  $\Delta = 90^\circ$  the CESR and spin waves occur in the gap between the fundamental and first subharmonic of the cyclotron waves. (See Fig. 8 and the following paper.) This situation exists only for a small angular region around  $\Delta = 90^\circ$ . By the time  $\Delta = 70^\circ$ , which is about the spin-wave critical angle, the background is becoming a problem.

The value of the critical angle and the separation of the spin waves from CESR at  $\Delta = 90^\circ$ , along with the linewidths of the observed peaks, constitute a set of data. Because  $\Delta_c$  depends only on the symmetry of the dispersion curve, it is independent of sample thickness. However, at  $\Delta = 90^\circ$ , the strong dependence of spin-wave location on sample thickness requires very accurate thickness determination in order to deduce accurate values for the Landau parameters.

### III. EXPERIMENTAL TECHNIQUE

#### A. Sample preparation

The experimental techniques are basically the same as in I. We include only what is special to

Rb, or necessary for a logical presentation.

The rubidium samples were made from material purified in this laboratory by heating very pure RbCl with calcium in a quartz vacuum system.<sup>9</sup> The Rb vapor given off traveled through several sets of baffles with a carefully controlled temperature gradient to trap impurities. The material was finally collected on a cold finger. When sufficient material was deposited, the cold finger was slightly heated. The rubidium melted and dropped into quartz ampules that were pulled off the system under vacuum. The ampules were refrigerated and stored for several years before use in these experiments. Comparison with preliminary experiments done at the time of purification indicate no gross deterioration of the material during storage.

To make a sample, an ampule was opened in a helium atmosphere dry box and the material transferred to an extruding device. Many samples could be made from one ampule. Motion of a piston forced the Rb through a slit in the end of the extruder. The dimensions of the slit were chosen to make a ribbon slightly thicker than the desired sample thickness. This ribbon was sandwiched between two microwave cavities, forming a common wall between them. A carefully made shim between the cavities was used to define the final sample thickness and assure parallelism of the sample surfaces. The samples were polycrystalline.

The cavity-sample assembly was removed from the dry box, fastened to the waveguide of the spectrometer, and plunged quickly into liquid nitrogen. It cooled rapidly to 250 K before the liquid boiled below the cavities. It further cooled to 100 K in about 1 h. Finally, liquid helium was added and the sample cooled to 4 K in 5–10 min. After one run the sample was allowed to sit for 24 h at 77 K to see if an annealing period would improve the momentum scattering and spin relaxation times. There was no difference between the signals before and after this annealing.

#### B. Cavities

Two sets of microwave cavities were used in this work. One set had both cavities tunable and contained no dielectric other than the ambient atmosphere. In these cavities the sample was pressed between two thin (0.14 mm) glass plates which made flat mirror surfaces on the Rb. The backs of these cavities could be removed and the thickness of the sample package directly measured at room temperature and 77 K, as described below.

The fact that the sample was bonded tightly to

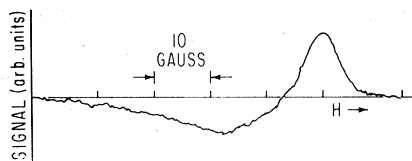


FIG. 4. CESR and first spin wave in sample Rb-6. The material is from the same ampule as that used for samples Rb-5 and Rb-7. This sample was pressed between glass plates in the tunable cavities. In contrast, the higher resolution signal in Fig. 1 was obtained with a sample (Rb-7) pressed between paraffin in the Lucalox-filled cavities.

glass introduced some serious problems in Rb. On cooling, the sample bulk contraction is much larger than that of the glass to which it was bonded, and thus the sample is strained at low temperature. Further, direct measurements indicate that the constraints resulted in a thickness contraction (the only dimension free to move) of about 2.5 times that expected based on the bulk (unconstrained) thermal contraction coefficients. This is discussed more fully below. This condition resulted in a broadening of both the CESR and the spin waves and made it impossible to get useful spin-wave data with these cavities. Figure 4 shows this signal.

Rb from the same ampule produced much better signals when run in the second set of cavities. Only one cavity of this set is tunable, and both contain the dielectric Lucalox. The Lucalox does not completely fill the cavity and the remaining volume is filled with a thin layer of paraffin ( $\approx 0.05$  mm) flush to the brass flanges of the cavities. Thus for these cavities the sample was pressed between wax rather than glass, and we surmise it was not as constrained. These cavities give better signals (compare Figs. 1 and 4), but it is not possible to directly measure the sample thickness.

Because thickness is such an important parameter in these measurements, a great deal of effort was expended to determine it. The final procedure involved using the tunable cavities to observe several thickness-dependent signals not related to the spin waves, and then comparing them to the same signals in the Lucalox cavities. This allowed determination of the relative sample thickness of the Lucalox cavity samples and is discussed in Sec. IV B 2. The absolute thickness of the tunable cavity samples was measured with the instrument described next.

#### C. Absolute sample thickness

The thickness of the Rb in glass sandwiches could be directly measured in the tunable cavities

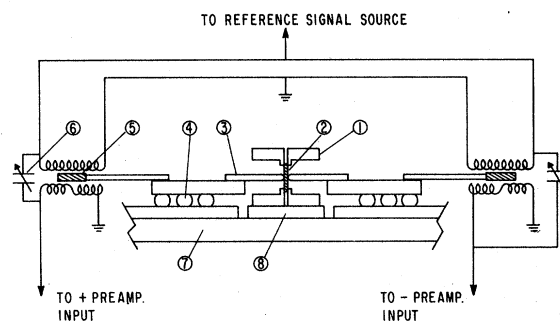
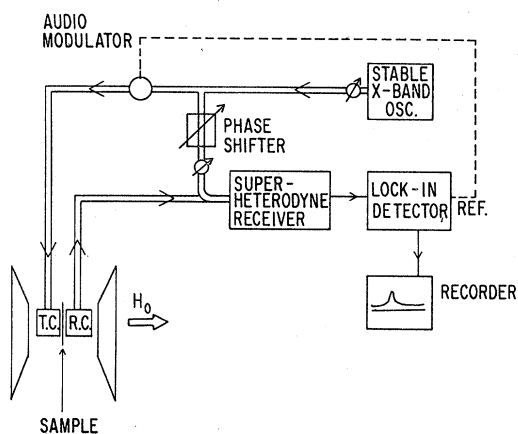


FIG. 5. Schematic representation of the device used to measure sample thickness. (1) Microwave cavity; (2) Sample; (3) Probe; (4) Ball bearing; (5) Armature; (6) Trim capacitor; (7) Brass Base Plate; (8) Removable cavity holder. Sliding the probes back allows removal of this holder with the cavities. It can be replaced by a holder containing calibration standards that are located very close to the same position as the sample.

with the device schematically shown in Fig. 5. Details will be published elsewhere.<sup>10</sup> It basically consists of a pair of linear variable differential transformers (LVDT) with the armatures mounted on carefully built kinematic suspensions. Long probes reach in and touch the glass surfaces of the sample package. Measurements can be made at 77 K by immersing the entire device in liquid nitrogen. Operation at low temperatures requires a dry atmosphere to prevent condensation of atmospheric moisture into the nitrogen, so the apparatus is operated in a simple dry box. Primary calibration at room temperature is with machinist gage blocks, whose thicknesses are known to  $\pm 0.02$   $\mu\text{m}$ . Low-temperature calibration is done using quartz plates previously calibrated at room temperature, since quartz does not change thickness significantly on cooling. Because this is a contacting measurement, dust and very small particles are the major sources of error. With sufficient care, the thickness can be determined to  $\pm 0.25$   $\mu\text{m}$ .

#### D. Spectrometer

Figure 6 shows a block diagram of the microwave transmission spectrometer used in these experiments. Details will be published separately. Microwave power from a stable oscillator is chopped at an audio frequency and coupled into the transmitting microwave cavity. A precision attenuator is used to set the power level. The cavities are located in a Dewar system in the gap of an electromagnet. Use of various cryogenic liquids and a feedback temperature control system allow operation from room temperature to 1.4 K. Microwave power that is transmitted through the sample enters the receiving cavity and goes to a



Block Diagram of Transmission ESR

FIG. 6. Block diagram of the microwave transmission spectrometer. TC and RC are, respectively, the transmitting and receiving cavities.

super heterodyne detector. A maser preamplifier<sup>11</sup> is available to boost the transmitted power and reduce the effective noise from the balanced mixer, from 2500 K to on the order of 100 K.

Coherent, unmodulated power is added to the transmitted power before amplification. This produces a strong i.f. carrier that biases the detector crystal and also provides a reference field with which to compare the transmitted field. The phase of this reference field can be adjusted by a precision phase shifter and the amplitude is set by a precision attenuator. The output of the i.f. amplifier is finally detected by a lock-in amplifier. Because of the low signal levels it is very important to avoid microwave leaks that might swamp the signal. Typically there is 160-dB isolation between the transmitter and receiver.

The externally applied magnetic field is horizontal and it can be rotated relative to the sample either manually or with a variable speed motorized drive.<sup>12</sup> The modes in the microwave cavities are arranged so the rf magnetic field is perpendicular to the dc field at all magnet orientations. Angular displacements of the dc field can be electronically<sup>12</sup> measured to  $0.01^\circ$ . Absolute orientation of the field relative to the sample can be determined by looking at the symmetry of some angularly dependent signal like that shown in Fig. 10. The point where the field is parallel to the sample surface can be determined to  $\pm 0.05^\circ$  in this way.

There is no absolute phase standard in transmission experiments, so phase must be measured relative to some signal. In this work phase was defined relative to the CESR signal at  $\Delta = 0^\circ$  (magnetic field perpendicular to the sample). Before any measurement was made that required knowledge of the phase, the magnet was rotated to

$\Delta = 0^\circ$  and the CESR antisymmetrized. This angle was chosen because the spin wave is typically farthest from the CESR at this position and is least likely to interfere. Proper phase for antisymmetrization could be set to  $\pm 1^\circ$ . It was assumed (as supported by separate experiments using narrow signals in lithium) that the effective phase of the spectrometer does not change with magnet angle. Changing helium levels in the Dewar caused continuous phase drift, so phase was checked before and after important measurements.

#### IV. DATA

##### A. Basic analysis technique

Figure 7 shows the analysis of a set of simulated data. It demonstrates the ability of spin-wave measurements to determine the Landau parameters and shows the sensitivity of the Landau-parameter measurements to uncertainties in sample thickness. The data, consisting of the critical angle, the separation of the CESR and first spin wave at  $\Delta = 90^\circ$  and  $\Delta = 0$ , and the linewidths of the CESR and first spin wave were obtained from a set of line shapes generated using Eq. (3), evaluated with values of the various parameters representative of the alkali metals.

The curves in the  $B_0$  vs  $B_1$  plane shown in Fig. 7

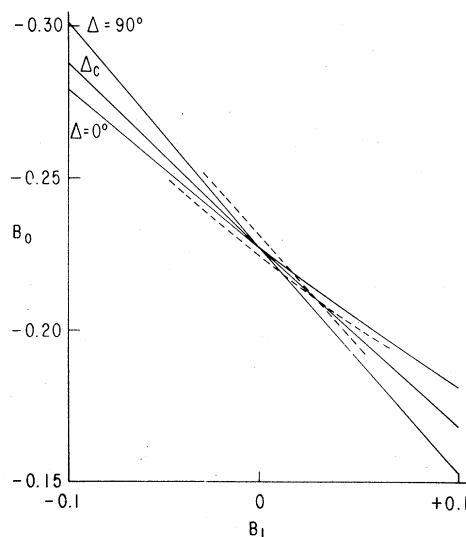


FIG. 7. Analysis of simulated data using the PW theory. The  $B_0$  vs  $B_1$  relations consistent with the data are shown at the three angles where data is normally taken. All three lines intersect at one point, which gives back the values of  $B_0$  and  $B_1$  used originally to generate the simulated data. The dotted lines show the effect of analyzing the same data using a thickness 1% thicker than that used originally to generate it.

were determined in the following way. At  $\Delta = 90^\circ$  and  $B_1 = -0.1$ , for example, values of  $B_0$  and  $\tau$  which resulted in a spin-wave line shape with the correct separation and linewidth were found by iteration.  $T_2$  is chosen to give the correct CESR linewidth and has little effect on the spin-wave peak. The same was done for  $B_1 = 0$  and  $B_1 = +0.1$ .  $B_0$  and  $B_1$  values from any point on this curve will fit the  $\Delta = 90^\circ$  data. The value of  $\tau$  needed to fit the linewidth varies slightly along the curve. Table IV shows the results of this procedure for the real samples. This was repeated at  $\Delta = 0^\circ$ . The intersection of the curves gives the values of  $B_0$  and  $B_1$  that were used to originally generate the data. To determine the  $B_0$  vs  $B_1$  relation consistent with the critical angle, we found the value of  $B_0$  that for a given  $B_1$  (and  $\tau$  from the  $\Delta = 90^\circ$  analysis for that  $B_1$ ) gave a line shape that was symmetric about the CESR field.

It is important to note that the angle of intersection of these curves is small. Any experimental uncertainty can be visualized as a broadening of the individual lines and thus the intersection will not be a point, but occur over some elongated region approximately parallel to the lines. Although the individual uncertainty in  $B_0$  and  $B_1$  will be large, the area of the  $B_0$  vs  $B_1$  plane consistent with the spin-wave data will be small.

The dotted lines in the figure show the result of analyzing the simulated data using a thickness 1% thicker than that used to generate it.  $B_0$  and  $B_1$  are very sensitive to this small change. Note that the lines intersect on the original line based on the critical-angle data. This demonstrates the independence of the critical angle from sample thickness.

In view of this extreme sensitivity to sample thickness, it is important that thickness be determined accurately. We have previously mentioned that the signals observed using the cavities in which it was possible to directly measure the thickness are of low quality. For the Lucalox filled cavities, which give the better signals, it was necessary to use indirect methods to determine the thickness of the samples. This is discussed below in two parts, the first dealing with absolute measurements of the thickness of the samples bonded to glass windows; and the second with the method of determining the thickness of samples in the Lucalox filled cavities relative to those that were directly measured.

## B. Sample thickness

### 1. Absolute measurement

The ability to very accurately measure the thickness at one point of the glass-alkali-glass sample

package in the double tunable cavities allowed the direct measurement of the thermal contraction of the Rb between room temperatures and 77 K. The results, compared with the free bulk contraction, are presented in Table I. This gives an indication of the strain in the samples. The deformations appear to be elastic because several temperature cycles repeat the same results. The measured contractions apply to samples about 1 cm square with about a 0.2-mm thickness of alkali metal. Including the errors in measuring the glass window thickness, the sample thickness could be determined to 1%, with an additional 1% nonuniformity in any one sample possible.

The sample thicknesses used were measured at 77 K. If the same enhancement of thermal contraction seen between room temperature and 77 K continues to 1 K, the samples would be an additional 0.8% thinner. We have standardized the data analysis of Sec. V to the 77-K thickness since we do not know whether this additional contraction really occurs. Enough information is presented in Sec. V to recalculate the Landau parameters with this reduced thickness if desired.

### 2. Relative thickness determination

Three different signals were used to compare the thicknesses of the samples. Two of them, the cyclotron waves and some strongly angularly dependent oscillations, were found to agree and give consistent results. The third, the Gantmakher-Kaner oscillations, gave erratic results, never in agreement with the others. Table II summarizes the thickness determinations. More detailed information on each of these signals is presented in the following paper.

*a. Cyclotron waves.* Figure 8 shows the transmission through a slab of rubidium at  $\Delta = 90^\circ$  between 4 and 6.5 kG. All the alkalis are similar. Above 8 kG there is no detectable transmission. This signal that starts at the cyclotron field  $H_c$  is the fundamental of the cyclotron waves. The subharmonics start at the fields  $H_c/2$ ,  $H_c/3$ , etc. No rigorous line-shape formula for the transmission exists, although the dispersion relation has been

TABLE I. Thermal contractions of free and constrained alkali-metal samples.

	Bulk contraction <sup>a</sup> (%) to 77 K	Measured contractions (%) to 77 K
Na	1.31	3.4 ± 0.4
K	1.82	4.3 ± 0.3
Rb	1.84	5 ± 0.3

<sup>a</sup> Reference 29.

Table II. Absolute and relative thicknesses of the samples.

	Direct measurement (mm), 77 K	Angular wiggles	Plasma waves	Gantmakher-Kaner	Inferred thickness (mm), 77 K
$L_6$	$0.173 \pm 0.002$				
$L_8$	$0.179 \pm 0.002$				
$L_6/L_8$	0.965	0.977			
$L_7/L_5$		1.085	1.096	0.975	
$L_5/L_6$		0.905		0.875	
$L_5/L_8$		0.884	0.884		
$L_7/L_6$		0.984		0.85	
$L_7/L_8$		0.960	0.970		
$L_5$					$0.1575 \pm 0.0025$
$L_7$					$0.1700 \pm 0.0025$

carefully investigated, including many-body effects.<sup>7,13-16</sup> The situation is dealt with more fully in the following paper.<sup>17</sup>

Figure 9 shows a plot of the zero crossings of this signal in Rb as a function of magnetic field. The slight deviation from linearity at low field is expected (as well as deviations at the high-field end). For the present purposes, we have empirically found that the slope of this linear region is proportional to sample thickness. By changing temperature it is found that the slope is independent of  $\omega\tau$  over the range of variation encountered in the samples in this work. It also turns out to give consistent scaling when compared with the angular signals of Fig. 9(b).

*b. Angular signals.* If the field is swept higher in Fig. 8 there is no detectable transmission from 8 to 20 kG, which is the highest field available in our experiments. However, if the magnetic field is held at a constant magnitude (greater than 10 kG at X-band frequencies) and rotated away from  $\Delta = 90^\circ$ , several previously unreported transmission modes are found. They are characterized by different angular dependences at constant field, and

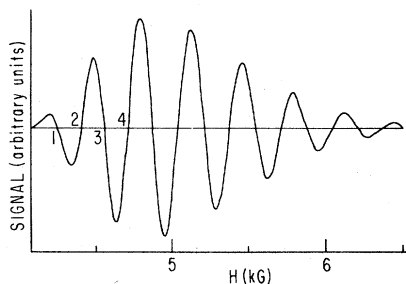


FIG. 8. Signal identified as the main harmonic of the plasma waves in sample Rb-7. The numbers of the zero crossings correspond to those of Fig. 9.

field dependences at constant angle. So far they have been observed in Na, K, and Rb. A more complete description is in the following paper, but as one mode was used for the sample thickness determinations, its relevant features will be described.

Figure 10 shows the transmission through a Rb sample as a function of angle  $\theta$  between the magnetic field and the sample surface for two constant values of the magnetic field. Note that the peaks are larger at the higher field, but are in the same locations. This is true for any field. If the angle is held constant and the field swept, the transmission slowly increases in magnitude (with

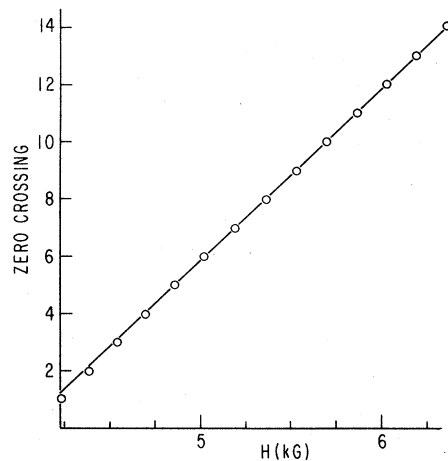


FIG. 9. Number of the zero crossing vs magnetic field for the plasma waves of Fig. 8. An increase of 1 corresponds to a phase change of  $\pi$  in the transmitted signal. Note the slight deviations from linearity at low field. Experimentally we find this slope is insensitive to changes in  $\omega\tau$  over the range encountered in samples in these experiments. Sample Rb-7, thickness  $\cong 0.17$  mm,  $\nu \cong 9.2$  GHz.

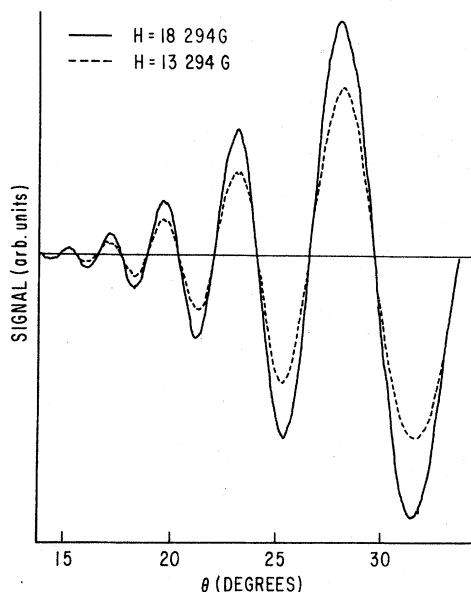


FIG. 10. Angular signals as a function of angle at two values of the magnetic field. Note the signals get stronger at high field, but the positions of the peaks and zero crossings are unchanged. There is also no change in peak positions if the temperature is changed. Sample Rb-7,  $L \cong 0.17$  mm,  $\nu \cong 9.2$  GHz.

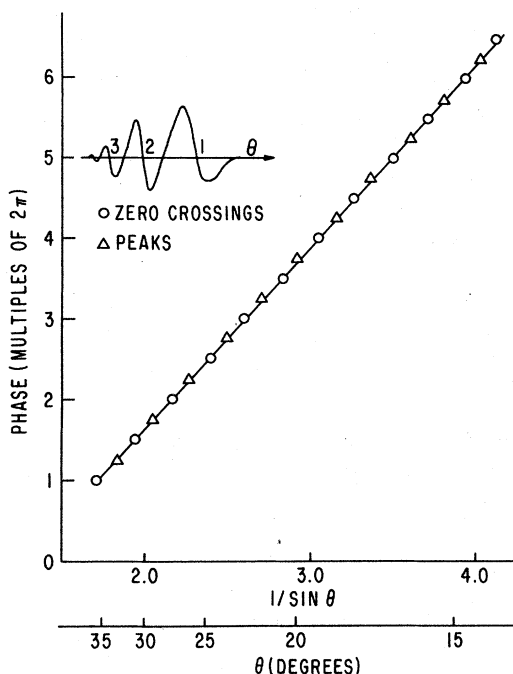


FIG. 11. Phase of the angular signals as a function of  $1/\sin\theta$  and  $\theta$ .  $\theta$  is the angle of the magnetic field relative to the surface of the sample. The inset shows the numbering scheme. Sample Rb-7,  $L \cong 0.17$  mm,  $\nu \cong 9.2$  GHz.

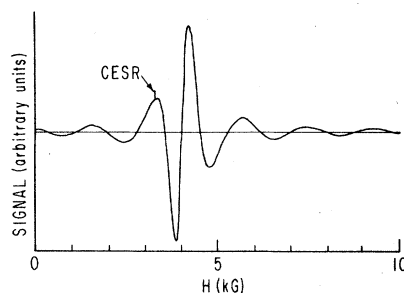


FIG. 12. Transmitted microwave field as a function of dc field through sample 7 at  $\Delta = 0^\circ$ . The reference phase has been adjusted to yield a symmetric CESR signal. This almost antisymmetrizes the large response at about 4 kG, the center of which is identified with the magnetic field corresponding to cyclotron resonance. The subsidiary signals at lower and higher fields are believed to be Gantmakher-Kaner oscillations. The inset to Fig. 13 shows these oscillations for sample Rb-5 between 10 and 20 kG.

some small superimposed oscillations) as the field is increased. The phase is unaffected by field strength. Raising temperature to decrease  $\tau$  weakens the signal but does not shift the peaks.

Figure 11 shows that a graph of the position of the peaks and zero crossings as a function of  $1/\sin\theta$  results in a very good straight line. We believe this is a mode discussed by Konstantinov and Skobov.<sup>18</sup> They show that the phase  $\varphi$  of the transmitted signal should be given by  $\varphi = \omega L/v_F \sin\theta$ .

In sodium this dependence is quantitatively correct using measured values for  $\omega$ ,  $L$ ,  $v_F$  from  $k_F$ , and  $m^*/m$ , and measuring the slope of the phase versus  $1/\sin\theta$  curve. In Rb this is not quantitatively true, but the slope is proportional to  $L/\sin\theta$ .

*c. Gantmakher-Kaner oscillations.* Figure 12 shows the transmission through a rubidium sample at  $\Delta = 0^\circ$ . The big peak occurs at the field where cyclotron resonance is expected. The precise mechanism for this is not known.<sup>19</sup> The oscillations above the peak continue on to the highest magnetic field available to us, 20 kG, as shown in the inset to Fig. 13. We believe these are Gantmakher-Kaner oscillations,<sup>20</sup> whence the magnetic field spacing for one complete oscillation should be given by  $\Delta H = 2\pi\hbar k_F c/Le$ , where  $\hbar k_F$  is the Fermi momentum,  $c$  is the speed of light,  $e$  the charge on an electron, and  $L$  the sample thickness. This is the increment in field that allows those electrons moving with  $\vec{v}_F$  essentially parallel to  $H$  to complete one additional cyclotron orbit on their way across the sample. As best as can be determined experimentally by changing temperature, the spacing is independent of  $\tau$ . This equation has been verified in potassium in samples whose thicknesses were directly measured.

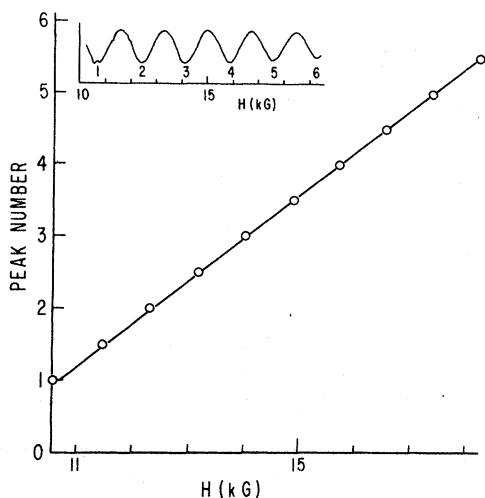


FIG. 13. Peak number of the Gantmakher-Kaner oscillations vs magnetic field. The inset shows the signal and numbering scheme. Note the slight deviation from linearity at low field. Sample Rb-5,  $L \cong 0.17$  mm,  $\nu \cong 9.2$  GHz.

Figure 13 is a graph of the peak number of these oscillations versus magnetic field in Rb. Note that the low-field points deviate slightly from a straight line drawn through those at the highest field. The slope also turns out to depend slightly on spectrometer phase. These deviations may be due to the tail left over from the big peak at cyclotron resonance. Using values for  $k_F$  from dHvA measurements<sup>6</sup> and the measured sample thicknesses, the above equation is not obeyed within experimental uncertainty in Rb. What is more important, the signal does not give consistent results when used for determining the relative thicknesses, (see Table II) and for this reason was not used. The following article contains more information about this signal.

*d. Sample geometry.* Sample size can have measurable effect on spin resonance line-shapes when relaxation times are long enough so the characteristic attenuation length of the transmission mode is comparable or larger than the dimensions of the cavity.<sup>21-24</sup> In Rb the relaxation

times are short enough so no geometrically induced signal anomalies were observed.

*e. Spin-wave data.* In Fig. 1 we presented a typical spin wave signal from one of the two Rb samples run in the Lucalox cavities on which accurate data were taken. The relevant measurements on these signals are summarized in Table III. In addition, two samples were run whose thicknesses could be directly measured. The thickness information on the samples is summarized in Table II. In Sec. V we will discuss the analysis of this data to extract the Landau parameters.

## V. ANALYSIS

Analysis of the Rb data presents some problems not found in Na and K. To lay the groundwork for this analysis we will first compare the behavior of the PW and WF calculations and examine how well the theoretical calculations reproduce the behavior of real spin-wave signals as a function of  $\tau$ .

### A. Comparison of PW and WF

As previously stated, the PW and WF calculations are equivalent to order  $q^2$ , but while the PW formulation has a relatively simple analytic form, the WF formulation is very complicated, especially at angles away from  $\Delta = 0^\circ$  and  $\Delta = 90^\circ$ . We have made comparisons between the theories, as discussed below, which indicate that given the uncertainties in the data it is not worthwhile to program the WF calculation for angles other than  $0^\circ$  and  $90^\circ$ . We will only use the WF calculation to fit the second spin wave at  $\Delta = 90^\circ$  in order to extract a value for  $B_2$ . The rest of the analysis uses the PW  $q^2$  approximation.

In Fig. 14 we compare the PW and WF analysis of the same simulated data that was used to generate Fig. 7. Sample thickness approximates that of the actual samples. Note that at  $\Delta = 90^\circ$ , which is where we have accurate data in Rb, the  $B_0$  vs  $B_1$  relations are essentially the same. Thus we can use the PW calculation in analyzing the first spin-wave data at  $\Delta = 90^\circ$ .

TABLE III. Experimental spin-wave data.

Sample	Temperature (K)	Thickness (mm)	$\Delta = 90^\circ$ Linewidth (G)	First spin-wave separation (G)	$\Delta = 90^\circ$		$\Delta_c$ (deg)	Frequency (GHz)
					Relative amplitude	Second spin-wave separation (G)		
5	1.4	$0.1575 \pm 0.0025$	18.8	$-21.88 \pm 0.2$	-0.19		$67.8 \pm 0.5$	9.189645
7	1.4	$0.1700 \pm 0.0025$	13.6	$-19.86 \pm 0.2$	-0.22	$-76.7 \pm 1$	$68.0 \pm 0.5$	9.19552
	2.15	$0.1700 \pm 0.0025$	16.3	$-18.61 \pm 0.2$	-0.19			9.2216

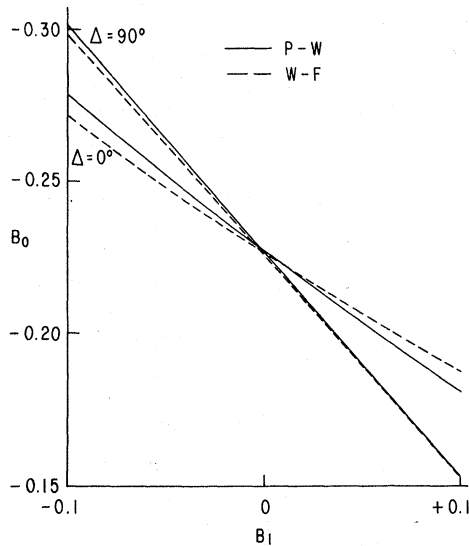


FIG. 14. Comparison of the WF and PW analysis of the same simulated data used to generate Fig. 7. Note that at  $\Delta=90^\circ$ , the two calculations are much closer than at  $\Delta=0^\circ$ .

Although direct comparison of the two theories utilizing calculations of the full line shapes is very difficult at other angles, it is straightforward to compare the two dispersion relations in the limit of infinite  $\tau$  and  $T_2$ . Figure 15 shows the dispersion relations as a function of angle for sev-

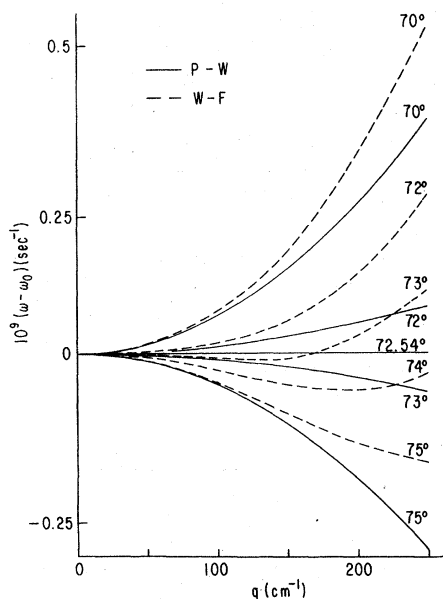


FIG. 15. Comparison of the infinite  $\omega\tau$  and  $T_2$  dispersion relations of PW and WF as a function of angle near the critical angle. Note that terms higher than order  $q^2$  are beginning to be important by  $q=100\text{ cm}^{-1}$ .

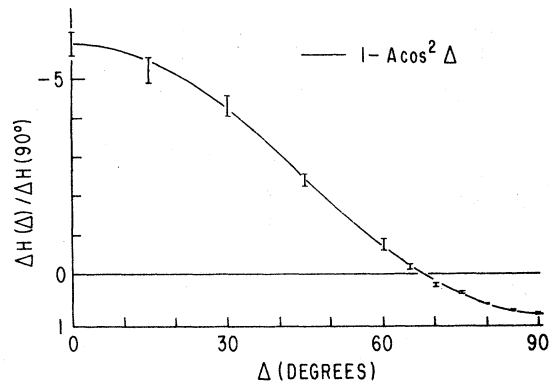


FIG. 16. Ratio of the separation of the first spin-wave peak at arbitrary  $\Delta$  to that at  $\Delta=90^\circ$  in sample Rb-7. The solid line is Eq. (7) normalized to fit the observed critical angle.  $A = [2m(1+B_1)/gm^*X_1]^2$ .

eral angles near the critical angle. Note that for small  $q$  they agree, while at larger  $q$  the presence of the higher-order terms in the complete calculation contributes significantly. For the samples used in these experiments,  $q$  corresponding to the first spin-wave peak is  $\approx 180\text{ cm}^{-1}$ . For this value of  $q$  it appears that the angle that could most reasonably be called the critical angle

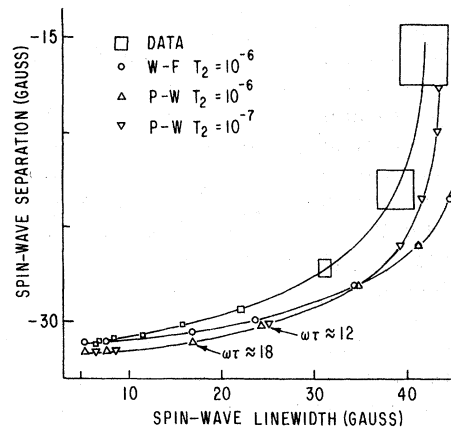


FIG. 17. Comparison of experimental measurements and computer calculations for the  $\Delta=90^\circ$  first spin-wave separation from CESR vs its linewidth. The data is from sample Na-16,  $L \approx 0.17\text{ mm}$ ,  $\nu \approx 9.2\text{ GHz}$ , and covers the range 1.4–12 K. The sizes of the square boxes represent the experimental errors. The analysis used  $B_0 = -0.215$ ,  $B_1 = -0.005$  and adjusts  $L$  to fit the low-temperature data using the WF theory. The same  $L$  is used in the PW analysis. Note that neither PW nor WF follows the experimental curve, although the PW calculation would come closer if the thickness were changed to match theory and experiment at low temperature. The theoretical curves for two values of  $T_2$  indicate that the effect of the CESR on the spin-wave separation is only important at relatively low  $\omega\tau$ .

TABLE IV. Analysis of  $\Delta = 90^\circ$  first spin-wave data.

Sample	Temperature (K)	Thickness (mm)	$B_1$	$B_0$	$10^{10} \tau$ (sec)	Amplitude	Phase shift (deg)
5	1.4	0.1550	-0.1	-0.3013	2.05	-0.17	-0.67
			0	-0.2266	1.92	-0.17	-0.55
			+0.1	-0.1533	1.81	-0.17	-0.47
		0.1600	-0.1	-0.3097	2.05	-0.17	-0.76
			0	-0.2377	1.88	-0.17	-0.64
			+0.1	-0.1665	1.77	-0.17	-0.54
7	1.4	0.1675	-0.1	-0.3061	2.70	-0.23	-0.76
			0	-0.2345	2.44	-0.23	-0.64
			+0.1	-0.1622	2.28	-0.23	-0.54
		0.1725	-0.1	-0.3144	2.65	-0.23	-0.86
			0	-0.2435	2.43	-0.23	-0.72
			+0.1	-0.1728	2.27	-0.23	-0.62
7	2.15	0.1675	-0.1	-0.3013	1.99	-0.18	-0.74
			0	-0.2266	1.90	-0.18	-0.60
			+0.1	-0.1533	1.79	-0.18	-0.50
		0.1725	-0.1	-0.3104	2.01	-0.18	-0.84
			0	-0.2377	1.83	-0.18	-0.70
			+0.1	-0.1657	1.72	-0.18	-0.59

for the PW theory is  $72.54^\circ$ , while that for the WF theory is on the order of  $73^\circ$ . Because our ability to experimentally determine the critical angle is limited by background signals to  $\pm 0.5^\circ$ , this is not

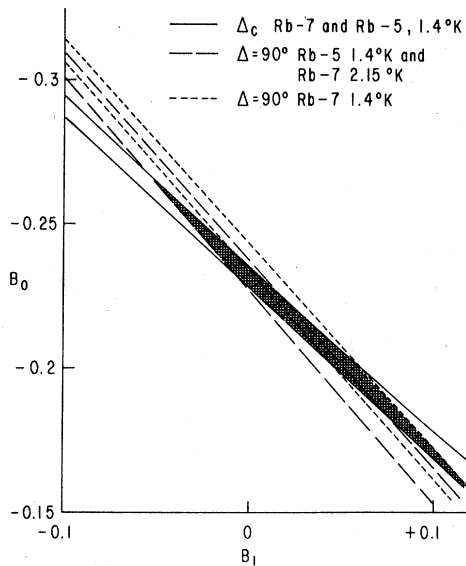


FIG. 18.  $B_0$  vs  $B_1$  relations based on the  $\Delta = 90^\circ$  first spin wave and the critical angle in samples Rb-5 and Rb-7. The two lines for each measurement represent the extremes due to uncertainties in the sample thickness (at  $\Delta = 90^\circ$ ) or the determinations of  $\Delta_c$ . The critical angle data from both samples yield essentially the same curves and so the two samples are not differentiated. The 1.4-K,  $\Delta = 90^\circ$  relations of Rb-5 are the same as the 2.15-K relations of Rb-7, so again they are not differentiated. The large shaded area shows the values of  $B_0$  and  $B_1$  we quote in our results.

a significant deviation. However, it should be kept in mind that the use of the  $q^2$  approximation at the critical angle is a possible source of systematic error in the analysis because of the finite  $\omega\tau$  and  $T_2$  in actual samples.

The measured critical angle, as defined by the angle at which the transmission is symmetric when phase is set by our convention, (symmetrize the  $\Delta = 0^\circ$  CESR) does depend slightly on  $\omega\tau$ . Computer simulations (and analytical calculations) show the deviation of the critical angle from its value at infinite  $\omega\tau$  is proportional to  $1/(\omega\tau)^2$ . The measured critical angles on samples with different  $\omega\tau$ 's are consistent with this dependence.

Figure 16 shows the separation of the first spin wave from CESR in Rb as a function of the angle  $\Delta$ . The solid line is the prediction of the PW calculation, Eq. (6), at infinite  $\omega\tau$ , normalized to fit the observed critical angle. The data follow the theory very well, indicating that no dramatic deviations between the  $q^2$  and complete calculations are expected. The large uncertainties in the measurements between  $\Delta = 0^\circ$  and the critical angle are due to the background signals.

#### B. Dependence on relaxation times

The position of the spin-wave peaks may depend on the relaxation times  $\tau$  and  $T_2$ . If  $T_2$  is long enough so that the CESR and first spin-wave peak are well resolved, it will have no influence other than determining the linewidth of the CESR peak. However, the value of  $\tau$  does influence the spin-wave peak position as well as its width. In the data analysis  $\tau$  is primarily determined by fitting

the linewidth of the first spin wave. Figure 17 compares the experimentally implied  $\tau$  dependence of the first spin-wave separation and linewidth at  $\Delta = 90^\circ$  in sodium to the behavior of the PW and WF theories as a function of  $\tau$  via a graph of the separation versus linewidth of the first spin wave. The size of the boxes through which the upper curve is drawn indicate the experimental uncertainty in the measurements. Experimentally, progress along this curve was controlled by sweeping temperature from 1.4 to 12 K. Over this temperature range in sodium the observed CESR linewidth at  $\Delta = 90^\circ$  is actually *narrowing*<sup>1</sup> as  $T$  increases due to decrease of geometrically induced spurious broadening.<sup>24</sup> Consequently it is not contributing any interference.

An important feature of the spin-wave behavior is that at high  $\omega\tau$  the location of the spin wave becomes insensitive to the spin-wave linewidth. As  $\omega\tau$  decreases, the spin-wave peak begins to shift. The data for rubidium falls in the  $\omega\tau$  region, where the position is somewhat sensitive to  $\omega\tau$ .

The other two curves show the analogous results for calculations using both the PW and WF formulations. The curves were made using  $B_0 = -0.215$ ,  $B_1 = -0.005$  (Ref. 1) and adjusting  $L$  so the WF calculation fits the data at the lowest temperature. This procedure was used because the data was taken in the Lucalox-filled cavities to achieve highest  $\omega\tau$ , and consequently the thickness could not be directly measured. The  $\omega\tau$  needed to fit the data at the lowest temperature was  $\approx 60$ . The PW curve was generated using the same values of the parameters as in the WF calculation, so the difference between the curves show the difference between the  $q^2$  and full theories.

Neither curve follows the experiment exactly although the slope of the PW line more closely approximates the slope of the data. The discrepancies between the WF calculations and the data do not make significant differences in the analysis as long as  $\omega\tau$  is greater than 15 or so. This was the situation for the Na and K. If parameters are chosen to make the PW theory fit the data at high  $\omega\tau$ , then there is no significant  $\omega\tau$  dependence of the deduced Landau parameters down to  $\omega\tau \approx 12$ , although there is a slight difference between the PW and WF results. In Rb, the situation is not so simple. As will be seen, there is a significant  $\omega\tau$  dependence to the results and this will contribute some uncertainties to our conclusions. These problems could result from approximations in the Landau theory as applied to spin waves (neglect of spin orbit coupling, assumption of a spherical Fermi surface) or more mundane difficulties in generating a sufficiently accurate theoretical line-shape formula that in-

cludes all the complicated aspects of transmission resonance.

### C. Landau parameters

#### 1. $B_0$ and $B_1$

The analysis for the Landau parameters follows the procedure described in Sec. IV A. Table IV presents the results of calculations used to generate the  $B_0$  vs  $B_1$  relations determined by the spin-wave data at  $\Delta = 90^\circ$ . Results for the two Lucalox cavity samples on which we have accurate data are shown. These  $B_0$  vs  $B_1$  relations, which correspond to the extremes of the thickness measurement uncertainties, are graphed on dashed lines in Fig. 18. The values of the parameters used in the analysis were  $k_F = 0.695 \times 10^8$ ,<sup>6</sup> and  $m^*/m = 1.23$ .<sup>25,26</sup> The thicknesses are those from Table II.  $\tau$  was obtained by fitting the spin-wave linewidth. The amplitude is normalized to the CESR signal. As described previously, the phase of the spectrometer was defined relative to that of the CESR at  $\Delta = 0^\circ$ . The data analysis was done using the analogous procedure on the computer. The phase shifts of Eq. (3) necessary to antisymmetrize the CESR at  $\Delta = 0^\circ$  are shown in Table IV. These small phase shifts imply very little interference between the CESR and first spin wave.

At this point it is apparent that there is a problem with these results. The  $B_0$  vs  $B_1$  relations deduced from different samples with differing values of  $\tau$  and  $L$ , etc. should be essentially the same at a given  $\Delta$ . They should at least intersect at the values of  $B_0$  and  $B_1$  that are correct for the material. This does not happen. Figure 18 shows that the  $B_0$  vs  $B_1$  relations deduced from sample 7 at the two temperatures (with different  $\tau$ 's and  $T_2$ 's) differ significantly. The  $\tau$  dependence of the spin waves deviates more strongly from the theory in Rb than the previously discussed Na. The higher temperature data of sample 7 corresponds to about the same  $\tau$  (Table IV) as the 1.4-K data

TABLE V. Analysis of critical angle data.

Sample	Temperature	$\Delta$	$B_1$	$B_0$
	(K)			
5	1.4	67.3	-0.1	-0.2945
			0	-0.2350
			+0.1	-0.1780
		68.3	-0.1	-0.2875
			0	-0.2275
			+0.1	-0.1680
7	1.4	67.5	-0.1	-0.2948
			0	-0.2350
			+0.1	-0.1775

of sample 5. The  $B_0$  vs  $B_1$  relations deduced from these data are the same, even though the thicknesses are different. This indicates that the indirect thickness determining procedure is probably working well. In both of these samples,  $\tau$  and  $T_2$  are impurity limited at 1.4 K.

Table V gives the pairs of  $B_0$  and  $B_1$  values consistent with the measured critical angle in both samples. The solid lines in Fig. 18 are plots of these  $B_0$  vs  $B_1$  relations. The two lines represent the extremes of the uncertainties in the measurement. The curves for both samples are essentially the same and are not differentiated.

The large cross-hatched region in Fig. 18 indicates the possible  $B_0$  and  $B_1$  values consistent with our measurements. This large region is partially due to the apparent  $\tau$  dependence of the analysis. In Table VI we present the sensitivity of the analysis for  $B_0$  and  $B_1$  to small changes in the other parameters. The calculations are done

TABLE VI. Effect of parameter variations on  $B_0$ ,  $B_1$  analysis.

Angle	Variation (at constant $B_1$ )	Comments
$\Delta_c$	$\frac{\partial B_0}{\partial \phi} = -0.0011/\text{deg}$	Making $\phi$ more negative increases $B$ lobe on low-field side of CESR.
	$\frac{\partial B_0}{\partial L} = 0$	
	$\frac{\partial B_0}{\partial \tau} \cong 0$	
	$\left(\frac{\partial B_0}{\partial (m^*/m)}\right)_{v_F} = +0.11$	Equation (7) shows only $m^*/m$ enters.
	$\left(\frac{\partial B_0}{\partial v_F}\right)_{m^*/m} = 0$	
$90^\circ$	$\left(\frac{\partial B_0}{\partial (m^*/m)}\right)_{k_F} \cong 0$	
	$\left(\frac{\partial B_0}{\partial v_F}\right)_{k_F} \cong 0$	
	$\frac{\Delta B_0}{\Delta k_F} = k_F \frac{\partial B_0}{\partial k_F} = +0.34$	
	$\frac{\Delta B_0}{\Delta S/S} = S \frac{\partial B_0}{\partial S} = -0.16$	$S$ is the separation in gauss of the first spin wave from CESR and is negative.
	$\frac{\partial B_0}{\partial \phi} < 2 \times 10^{-3}/\text{deg}$	

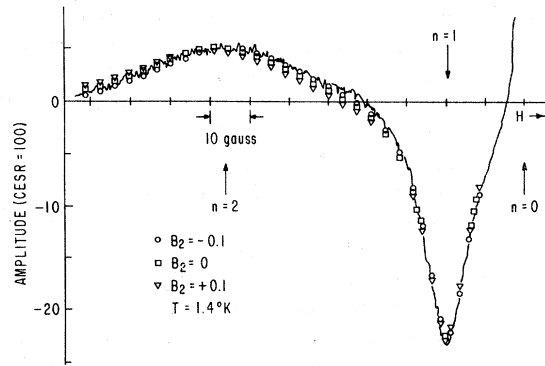


FIG. 19. Fit of the WF theory to the second spin wave as a function of  $B_2$  in Rb-7.  $B_0$ ,  $B_1$ , and  $\tau$  have been chosen to fit the first spin-wave position and linewidth when  $B_2=0$ .  $T_2$  is determined from the CESR width. A slight dependence of the first spin wave on  $B_2$  can be seen. The parameters for the fit are  $B_0 = -0.1832$ ,  $B_1 = 0.085$ ,  $L = 0.1725$  mm,  $\nu = 9.19552$  GHz,  $T_2 = 0.676 \times 10^{-7}$  sec,  $\tau = 2.39 \times 10^{-10}$  sec.

for  $B_1=0$  and for a thickness approximating those of the actual samples. For example, they can be used to adjust the  $B_0$  vs  $B_1$  relations of Fig. 18 to get a feel for the effect of using a different value for  $m^*/m$ .

## 2. $B_2$

Figure 19 shows a fit to the first and second spin wave of sample 7 using WF theory. The amplitude has been normalized to the CESR, which is not shown.  $T_2$  was determined from the CESR linewidth. Values of  $L$ ,  $\tau$ ,  $B_0$ , and  $B_1$  used for this figure are those from the one corner of the error parallelogram formed by the  $1.4^\circ$  data of sample 7 in Fig. 18. The general fit is excellent. The re-

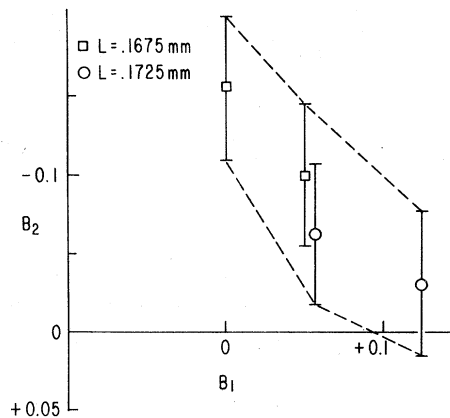


FIG. 20. Relation between  $B_2$  and  $B_1$  consistent with the second spin wave in Rb-7. The choice of a  $B_0$  and  $B_1$  from Fig. 18 implies the  $B_2$  for that  $B_1$  given by this figure.

sults are shown for three values of  $B_2$ , and a slight dependence on  $B_2$  is evident. Figure 20 shows the values of  $B_2$  that fit the second spin-wave position for  $B_0$ ,  $B_1$ ,  $\tau$ , and  $L$  values from all four corners of the error parallelogram of the lowest temperature data from sample 7.

The error bars in Fig. 20 have two components, one due to the uncertainty in the measurements of the second spin-wave position and the relative insensitivity of the fit to  $B_2$ , and the other due to the uncertainty in measurements of the first spin-wave position (approximately 1%). This 1% uncertainty is not a dominant error source for the  $B_0$  and  $B_1$  measurements, but since the second spin wave is much more sensitive to  $B_0$  than to  $B_2$  (Table VII), it results in a significant contribution to the error in the determination of  $B_2$ . Table VII shows the sensitivities of the positions of the first and second spin waves to  $B_0$  and  $B_2$  (at constant  $B_1$ ) as well as the effect of changing  $m^*/m$  on the separation of the second spin wave.

From Fig. 20 it would appear that  $B_2$  is most probably negative. If it is taken close to zero,  $B_1$ , must be large and positive. Changing  $m^*/m$  to 1.20 and following this consistently through the analysis for  $B_0$  and  $B_1$ , and then  $B_2$ , would result in  $B_2$  values about 0.015 more positive. If the sample thickness is reduced to compensate for the possible contraction between 77 and 1.4 K, the probable values of  $B_2$  move more negative. In sodium and potassium the possible values for  $B_2$  were symmetric around zero.

In conclusion, the values of the Landau parameters consistent with the observed spin waves in Rb are  $B_0 = -0.21 \pm 0.05$ ,  $B_1 = +0.03 \pm 0.08$ , and  $B_2 = -0.09 \pm 0.1$ . The errors are not independent,

TABLE VII. Effect of parameter variations on first and second spin-wave separation at  $\Delta = 90^\circ$ .

Variation (at constant $B_1$ )	Comments
$\frac{\partial S}{\partial B_0} = -120$	$S(B_0, B_1, \dots)$ is the separation in gauss of the first spin wave from CESR and is negative.
$\frac{\partial F}{\partial B_2} = -1.5$	
$\frac{\partial G}{\partial B_0} = -400$	$G(B_0, B_1, \dots)$ is the separation in gauss of the second spin wave from CESR and is negative.
$\frac{\partial G}{\partial B_2} = -25$	
$\left( \frac{\partial G}{\partial (m^*/m)} \right)_{k_F} = -20$	

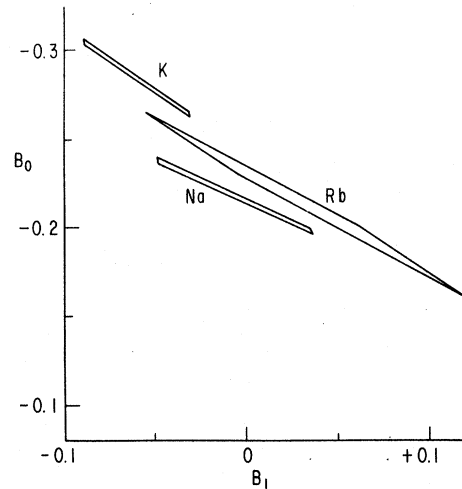


FIG. 21. Allowed regions of the  $B_0$  vs  $B_1$  plane consistent with the spin waves in the three alkali metals in which precision spin-wave measurements have been made. The region quoted for Rb is the shaded area shown in Fig. 18.

as shown in Figs. 18 and 20. Additionally, there may be systematic errors in these results. We have discussed at length three of the major possible sources: the indirect sample thickness determinations, the use of the PW rather than WF analysis at  $\Delta_c$ , and the apparent  $\tau$  dependence of the  $\Delta = 90^\circ$  analysis.

## VI. DISCUSSION

The only other experimental Landau-parameter determinations in Rb with which we are familiar is the dHvA measurement of Knecht, Randles, and Shoenberg<sup>27</sup> and, more recently, that by Knecht.<sup>28</sup> Knecht determined  $B_0 = -0.295 \pm 0.012$ . Considering the complexity of our measurements, we regard this as quite satisfactory agreement. In comparison, we note that although the dHvA and spin-wave results virtually coincide for K, the difference for Na is comparable to that for Rb.

The dHvA and spin wave measurements are complementary. A more accurate measurement of  $B_0$  from dHvA data, or some other source, can result in a more accurate value of  $B_1$  using the relation in Fig. 18, as the spin waves determine the relation between  $B_0$  and  $B_1$  more accurately than they determine either of them individually. We believe that given the uncertainties in our work, as previously discussed, it is best to use the  $B_0$ - $B_1$  relation as determined from the critical-angle data. Following such a selection for a value of  $B_1$ , a better value of  $B_2$  can be obtained via Fig. 20.

If one regards the correct value of  $B_0$  to be

closer to the dHvA result, we would find from Fig. 18 that  $B_1 \approx -0.1$ . From Fig. 20 we see this would imply a large (negative) value for  $B_2$ . However, since the  $B_1$ - $B_2$  relation is sensitive to the details of the line-shape fitting, and as the dHvA value is outside of that used to determine Fig. 20, this conclusion must be regarded with appropriate caution. On the other hand, the value of  $B_1$ , being deduced from the critical-angle relationship, can be regarded with more confidence.

In Fig. 21 we present the values of  $B_0$  and  $B_1$  consistent with the spin-wave observations in the three alkali metals for which precision measurements have been made. For Na and K the results agree well with theoretical calculations of Rice.<sup>29</sup> For Rb, in particular, we can compare with the recent calculation of the electronic susceptibility by MacDonald and Vosko.<sup>30</sup> Using  $m^*/m = 1.23 \pm 0.02$ , and our  $B_0 = -0.21 \pm 0.05$ , we obtain for the ratio of the true susceptibility compared to the free-electron value  $\chi/\chi_0 = (m^*/m)/(1+B_0) = 1.56 \pm 0.1$ . Depending upon the details of the calculational methods, MacDonald and Vosko obtain values ranging from 1.73 to 1.98.<sup>30</sup> We are not qualified to comment on any significance to this difference, but do note that their corresponding results for Na and K agree very well with those deduced from the spin-wave values. Perhaps further theoretical efforts will resolve the matter.

The obvious way to improve the spin-wave measurements in the future would be to change the sample fabrication techniques. It would be necessary to work with strain-free single-crystal samples. Such samples could perhaps be made using an ion mill to machine flat parallel surfaces on single crystals clamped in holders at the edges. The samples could be thinned around the periphery to relieve the strains induced on cooling. A noncontacting method of thickness measurement would have to be used. The mechanical and chemical properties of the alkalis would make fabrication of these samples very difficult, but possible, should the effort be worthwhile.

We have observed spin waves in cesium similar in character to those in the other alkalis, but the apparent  $g$  value of the CESR shifts from run to run, probably due to strain in the samples. Thus Cs appears to be more strain sensitive than Rb (the strain in Rb seems to manifest itself most obviously in broadened linewidths for the CESR and spin waves). This coupled with the larger deviations from isotropy makes it not worthwhile to attempt precision spin-wave measurements in Cs until one is committed to making strain-free single-crystal samples. It would be interesting to study the pressure dependence of the signals in Cs as part of a complete program to measure its

spin properties. Because of its less spherical Fermi surface and greater spin-orbit coupling, it is possible that the spin-wave behavior in Cs might exhibit significant deviations from the PW and WF theories.

#### ACKNOWLEDGMENTS

It is a pleasure to acknowledge the assistance of others in this work. Much of the ESR apparatus and the basic sample preparation techniques were developed in conjunction with Professor G. L. Dunifer. We thank Professor D. Fredkin and Dr. J. Dobson for discussions which helped us understand the Landau theory and the theoretical aspects of the cavity size effects. C. A. Latham built much of the specialized apparatus used in these measurements. We thank Paul Schmidt for sharing his techniques of alkali metal purification with us. We appreciate the generous grant of computer funds from the Research Committee of the San Diego Division of the Academic Senate. This work was supported in part by NSF Grant No. DMR 74-24361.

#### APPENDIX

The essential features of the spin-wave collective mode can be seen in the following one-dimensional classical model. It corresponds to the  $\Delta = 0^\circ$  three-dimensional case where the spin-wave mode propagates parallel to the applied magnetic field and the electrons travel freely in spiral orbits along the field. The model consists of classical particles distributed uniformly along the  $z$  axis, half moving with velocity  $v$  and half with velocity  $-v$ . They correspond to the electrons at the Fermi surface of a real metal. Each particle contains a bar magnet of moment  $\mu$  fixed parallel to its axis of rotation. The ratio of the magnetic moment to angular momentum is  $\gamma$ . With no interactions between the moments, the system is assumed to have a static susceptibility  $\chi_0$ . To complete the model we introduce a velocity-dependent short-range interaction between pairs of particles that has the form of the magnetic part of the Landau interaction function,

$$E_{ij} = \left( f(|z_i - z_j|) + \frac{\vec{v}_i \cdot \vec{v}_j}{v^2} g(|z_i - z_j|) \right) \vec{\mu}_i \cdot \vec{\mu}_j. \quad (\text{A1})$$

The first term corresponds to the  $P_0(\cos\theta)$  term and the second to the  $P_1(\cos\theta)$  term in Eq. (2). When the wavelengths of the excitations under consideration are much greater than the spacing between the particles, we may define two macroscopic magnetizations  $\vec{M}_+(z)$  and  $\vec{M}_-(z)$ . For the

moment we will suppress the time dependence.  $\vec{M}_+$  is the magnetization due to those moments moving in the  $+z$  direction, and  $\vec{M}_-$  is due to those moving the other way. In terms of the magnetization distribution, the effect of the interactions can be described by a molecular field approximation. If the wave length of any excitation is much longer than the range of the forces described by  $f$  and  $g$ , the effective field felt by the two magnetization distributions in the presence of an externally applied field  $H_0$  is

$$H_{\text{eff} \pm}(z) = \vec{H}_0 - [\vec{M}_+(z) + \vec{M}_-(z)]B_0 \mp [\vec{M}_+(z) - \vec{M}_-(z)]B_1, \quad (\text{A2})$$

where

$$B_0 = \int_{-\infty}^{\infty} f(|z-z'|) dz'$$

and

$$B_1 = \int_{-\infty}^{\infty} g(|z-z'|) dz'.$$

$H_0$  will be taken in the  $z$  direction.

If the wavelength of a disturbance is on the order of the range of the interactions, additional terms appear which in the  $v \rightarrow 0$  limit lead to the spin waves found in insulators. To next order in this model they depend on the parameters

$$J_0 = \int_{-\infty}^{\infty} f(|z-z'|)(z-z')^2 dz'$$

and

$$J_1 = \int_{-\infty}^{\infty} g(|z-z'|)(z-z')^2 dz'.$$

They will be left out in all that follows.

If we define  $M = \chi H_0 = \chi_0 H_{\text{eff}}$ , the static susceptibility is given by  $\chi = \chi_0 / (1 + B_0 \chi_0)$ . Thus it is evident that in this model  $B_0 \chi_0$  (and similarly  $B_1 \chi_0$ ) correspond to  $B_0$  and  $B_1$  in a real electron system.

In terms of the effective field, the equations of motion for the two magnetization distributions are

$$\frac{\partial \vec{M}_+}{\partial t} = \gamma \vec{M}_+ \times \vec{H}_{\text{eff}+} - v \frac{\partial \vec{M}_+}{\partial z}, \quad (\text{A3})$$

$$\frac{\partial \vec{M}_-}{\partial t} = \gamma \vec{M}_- \times \vec{H}_{\text{eff}-} + v \frac{\partial \vec{M}_-}{\partial z}.$$

Substituting for  $H_{\text{eff}+}$  and  $H_{\text{eff}-}$ , adding and subtracting these two equations, and defining  $\vec{M}_+ + \vec{M}_- = \vec{M}$ , and  $v(\vec{M}_+ - \vec{M}_-) = \vec{J}_M$ , we get

$$\frac{\partial \vec{M}}{\partial t} = \gamma \vec{M} \times \vec{H}_0 - \frac{\partial \vec{J}_M}{\partial z}, \quad (\text{A4})$$

$$\frac{\partial \vec{J}_M}{\partial t} = \gamma \vec{J}_M \times H_0 - 2v\gamma(B_0 - B_1)\vec{M}_+ \times \vec{M}_- - v^2 \frac{\partial \vec{M}}{\partial z}.$$

$\vec{M}$  is the total magnetizations and  $\vec{J}_M$  is the magnetization current. The equations can be linearized by writing  $\vec{M}_\pm = \frac{1}{2}\vec{M}_0 + \delta\vec{M}_\pm = \frac{1}{2}\chi H_0 + \delta M_\pm$  and assuming that the deviations for equilibrium,  $\delta\vec{M}_\pm$ , are small.  $\delta\vec{M}_\pm$  to lowest order are in the  $x$ - $y$  plane only. The equations become

$$\frac{\partial \delta\vec{M}}{\partial t} = \gamma \delta\vec{M} \times H_0 - \frac{\partial \vec{J}_M}{\partial z}, \quad (\text{A5})$$

$$\frac{\partial \vec{J}_M}{\partial t} = \gamma \vec{J}_M \times H_0 [1 + (B_1 - B_0)\chi] - v^2 \frac{\partial \delta\vec{M}}{\partial z}.$$

After Fourier transforming, this system of equations has a solution if

$$q^2 = (\omega_0 - \omega)[\omega_0(1 + \beta) - \omega]/v^2, \quad (\text{A6})$$

where  $\beta = (B_1 - B_0)\chi$ . This dispersion relation has two roots. One starts near  $\omega = \omega_0$ , and in this region

$$q^2 = \frac{\omega_0 - \omega}{(v^2/\omega_0)(1 + B_0\chi_0)/(B_1 - B_0)\chi_0}. \quad (\text{A7})$$

This has the same dependence on  $v^2$ ,  $\omega_0$ , and  $(1 + B_0)/(1 + B_1)$  as the PW dispersion relation for  $\Delta = 0^\circ$ . [See Eq. (3).] PW contains some other factors of  $1 + B_0$  and  $1 + B_1$  due to modifications of the orbital motion of the electrons that have not been included in this model. It is clear that this spin wave is analogous to that in the conduction electrons of a real metal.

To order  $q^2$  the other branch of this dispersion relation also exists in the spin-wave theory for real metals (see Ref. 5 for details). It is characterized by small  $\vec{M}$  and large  $\vec{J}_M$  so in practice it is not possible to couple to it.

For the normal spin-wave branch (A7), the quantities  $\delta\vec{M}_+$  and  $\delta\vec{M}_-$  are always parallel to each other at each point. Their relative magnitudes depend on the value of  $q$ . This situation is shown in Fig. 22(a). Note that because the magnitudes of  $\delta\vec{M}_+$  and  $\delta\vec{M}_-$  are different (to first order the  $z$  components are equal) the full vectors  $\vec{M}_+$  and  $\vec{M}_-$  are not parallel and can exert a torque proportional to  $\vec{M}_+ \times \vec{M}_-$  on each other because of the interactions.

Because the total magnetization is rotating with angular frequency  $\omega$  in a reference frame stationary with respect to the  $z$  axis, the transverse components of the individual moments,  $\delta\vec{\mu}_+$  and  $\delta\vec{\mu}_-$ , must be rotating at frequencies Doppler shifted from  $\omega$  by  $\pm qv$  so they can contribute properly to the macroscopic magnetization. This is represented in Fig. 22(b).

The way these individual motions contribute to a coherent spin wave is shown in Fig. 23. Part (a) shows a snapshot of the transverse component of the magnetization at a time  $t$ . The tips of the magnetization vectors form a helix as a function of

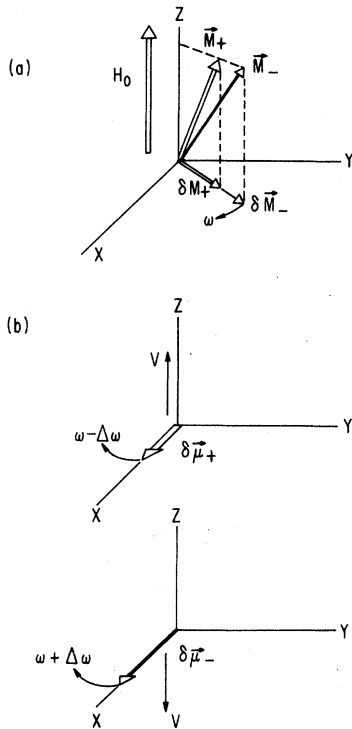


FIG. 22. (a) Magnetization vectors  $\vec{M}_+$  and  $\vec{M}_-$  at some point on the  $z$  axis. To first order, the  $z$  components of  $\vec{M}_+$  and  $\vec{M}_-$  are equal, but the  $x$ - $y$  components  $\delta\vec{M}_+$  and  $\delta\vec{M}_-$  are not.  $\delta\vec{M}_+$  and  $\delta\vec{M}_-$  are parallel and are rotating at angular frequency  $\omega$ . The individual moments  $\mu$  contributing to  $\vec{M}_+$  and  $\vec{M}_-$  at this particular location change continuously. (b)  $x$ - $y$  components  $\delta\vec{\mu}_+$  and  $\delta\vec{\mu}_-$  of the individual moments  $\vec{\mu}_+$  and  $\vec{\mu}_-$ . Again, to lowest order the moments are aligned with the  $z$  axis.  $\delta\vec{\mu}_+$  and  $\delta\vec{\mu}_-$  are moving in opposite directions and rotating at different angular frequencies, shifted by  $\pm qv$  from  $\omega$ . The two  $\delta\vec{\mu}$  shown are meant to be physically at the same location and thus they are drawn parallel. They have been separated for clarity.  $\delta\vec{M}$  at the location of these moments is parallel to them.

$z$ , as shown by the solid line. The transverse components of the individual moments are shown at three points. The short thick arrows are moving with velocity  $+v$ , while the long thin arrows are moving with  $-v$ . Note that at any  $z$ ,  $\delta\vec{\mu}_+$  and  $\delta\vec{\mu}_-$  are parallel, in accord with the discussion above. As time proceeds the three pairs of arrows shown separate. Each arrow rotates as it moves so it is always parallel to the arrow moving in the opposite direction with which it momentarily coincides. To see this in detail look at the two solid-head arrows in part (a) of the figure. They are moving in opposite directions so after some time  $\Delta t$  their  $z$  coordinates will coincide. Part (b) shows only these two arrows a time  $\Delta t/2$  after (a). Both arrows have rotated different amounts since they are precessing at different

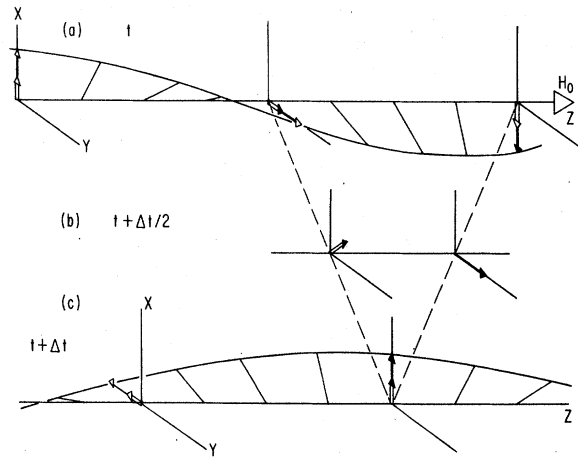


FIG. 23. (a) Snapshot of the spatial distribution of magnetization in a spin wave. The helical line shows the location of the tips of the vector  $\delta\vec{M}$  as a function of  $z$ . Every quarter wavelength the short arrows  $\delta\vec{\mu}_+$  and  $\delta\vec{\mu}_-$  are shown. Two arrows have solid heads and their motion will be followed through parts (b) and (c) of the figure. (b) Two solid head arrows at time  $\Delta t/2$  after the snapshot in (a). All others have been omitted for clarity. Their separation is half that in (a), and because of the different angular frequencies, they have rotated different amounts. (c) Two solid head arrows at the time when their spatial locations coincide. Note that they are parallel. All the arrows that have not been shown are undergoing this same motion. Again the helical line shows the locations of the tips of the vectors  $\delta\vec{M}$  as a function of  $z$ .

rates ( $\omega_{\pm} = \omega \mp qv$ ). For the figure  $qv/\omega = \frac{1}{3}$ . Part (c) shows that they are parallel when their spatial locations coincide. Also shown is the full outline of the transverse magnetization at this time. This spin wave is moving to positive  $z$  with phase velocity greater than the particle velocity  $v$ .

It is possible to derive (A6) using only the solution of the Bloch equations for a single spin in a static magnetic field. This helps bring out the essential physics involved in a spin wave. In the limit of infinite relaxation time, the Bloch equations say that the response  $\delta\vec{\mu}$  of a moment to a driving field  $\vec{H}_1$  at frequency  $\bar{\omega}$  is:

$$\delta\vec{\mu} = \gamma\mu_0\vec{H}_1/(\bar{\omega}_0 - \bar{\omega}). \quad (\text{A8})$$

$\mu_0$  is the  $z$  component of the moment and  $\bar{\omega}_0$  is the free precession frequency of the moment in the effective static field.  $\delta\vec{\mu}$  and  $\vec{H}_1$  are parallel and are in the  $x$ - $y$  plane.

In the present case,  $\vec{H}_1$  for the (+) moving spins is due to the  $x$ - $y$  components of  $M_-$ , and conversely for the negatively moving particles. The driving frequency felt by the plus moving spins is just the rotation frequency of the negative moving spins Doppler shifted by  $2qv$  because of their

relative motion. The sign of the Doppler shift changes when considering the negative moving particles. Equation (A2) shows that to first order, a moment  $\vec{\mu}_+$  feels an effective  $z$  component of the magnetic field equal to  $H_0[1 + (B_1 - B_0)\chi/2]$  and the appropriate  $\vec{H}_1 = (B_1 - B_0)\delta M_-$ . Requiring that the situation is self-consistent, i.e., (A8) is satisfied simultaneously for both sets of spins, leads to the dispersion relation (A6). Thus the fundamental picture of a spin wave shows that one group of spins is driven by the other, and it returns the favor. The situation is not totally symmetric (unless  $q=0$ ) since one distribution is being driven closer to its resonance frequency than the other (depending on the sign of  $q$ ), and thus its response per unit driving field is greater. In the self-consistent situation, its greater response is sufficient to excite enough  $\delta M$  in the other distribution to keep itself going.

Damping of the spin wave can come from two

sources. First, spin relaxation will cause the spin wave to die out. However, it is also clear from Fig. 23 that the internal motion in the spin wave is very well ordered and anything that disrupts this order will contribute to the damping. Importantly, momentum scattering will keep a particle from traveling properly and taking its correct place in the wave, thus disrupting the order. The graphs of Fig. 3 demonstrate this in a real case. Only in the region near  $\text{Re}(q)=0$  is the damping [proportional to  $\text{Im}(q)$ ] due to spin relaxation dominant. Recall that the dotted line asymptotes show the dispersion relation in the limit of infinite spin relaxation time. When  $\text{Re}(q)$  is small, an electron can go anywhere and still have the proper phase to contribute to the collective motion. As  $\text{Re}(q)$  increases, momentum scattering is more effective in dephasing the electron magnetization and quickly becomes the dominant damping mechanism.

\*Present address: Lawrence Livermore Laboratory, P. O. Box 808, Mail Code L-523, Livermore, Ca. 94550.

<sup>1</sup>G. L. Dunifer, D. Pinkel, and S. Schultz, *Phys. Rev. B* **10**, 3159 (1974). See also, G. L. Dunifer, Ph.D. thesis (University of California, San Diego, 1968) (unpublished); D. Pinkel, Ph.D. thesis (University of California, San Diego, 1974) (unpublished).

<sup>2</sup>L. D. Landau, *Zh. Eksp. Teor. Fiz.* **30**, 1058 (1956) [*Sov. Phys.-JETP* **5**, 101 (1957)].

<sup>3</sup>V. P. Silin, *Zh. Eksp. Teor. Fiz.* **33**, 495 (1957) [*Sov. Phys.-JETP* **6**, 387 (1958)].

<sup>4</sup>D. Pines and P. Nozières, *The Theory of Quantum Liquids* (Benjamin, New York, 1966), Vol. I.

<sup>5</sup>P. M. Platzman and P. A. Wolff, *Waves and Interactions in Solid State Plasmas* (Academic, New York, 1973).

<sup>6</sup>D. Shoenberg and P. J. Stiles, *Phys. Lett.* **4**, 274 (1963).

<sup>7</sup>P. M. Platzman and P. A. Wolff, *Phys. Rev. Lett.* **18**, 280 (1967).

<sup>8</sup>A. R. Wilson and D. R. Fredkin, *Phys. Rev. B* **2**, 4656 (1970).

<sup>9</sup>P. H. Schmidt (private communication).

<sup>10</sup>D. Pinkel (unpublished).

<sup>11</sup>L. Flesner, S. Schultz, and R. Clauss, *Rev. Sci. Instrum.* **48**, 1104 (1977).

<sup>12</sup>D. Pinkel and D. Eigler (unpublished).

<sup>13</sup>W. M. Walsh, Jr. and P. M. Platzman, *Phys. Rev. Lett.* **15**, 784 (1965).

<sup>14</sup>P. M. Platzman and W. M. Walsh, Jr., *Phys. Rev.* **19**, 514 (1967); (*E*) **20**, 89 (1968).

<sup>15</sup>P. M. Platzman, W. M. Walsh, Jr., and E-Ni Foo, *Phys. Rev. Lett.* **172**, 689 (1968).

<sup>16</sup>A. R. Wilson, Ph.D. thesis (Oxford University, 1968) (unpublished).

<sup>17</sup>Daniel Pinkel, Gerald L. Dunifer, and Sheldon Schultz, following paper, *Phys. Rev. B* **18**, 6658 (1978).

<sup>18</sup>O. V. Konstantinov and V. G. Skobov, *Fiz. Tverd. Tela.* **13**, 3323 (1971) [*Sov. Phys.-Solid State* **13**, 2792 (1972)].

<sup>19</sup>G. A. Baraff, *Phys. Rev. B* **9**, 4008 (1974), and references cited therein.

<sup>20</sup>V. F. Gantmakher and E. A. Kaner, *Zh. Eksp. Teor. Fiz.* **48**, 1572 (1965) [*Sov. Phys.-JETP* **21**, 1053 (1965)].

<sup>21</sup>J. F. Dobson and D. R. Fredkin (private communication).

<sup>22</sup>J. F. Dobson and D. R. Fredkin, *J. Low. Temp. Phys.* **18**, 13 (1975).

<sup>23</sup>J. F. Dobson, *Phys. Lett. A* **44**, 171 (1973).

<sup>24</sup>D. Pinkel and S. Schultz, *J. Magn. Res.* **22**, 509 (1976).

<sup>25</sup>This value is deduced from the position of the  $\Delta = 0^\circ$  big peak resonance. See the following paper. This is close to the Azbel-Kaner cyclotron measurement,  $1.20 \pm 0.02$  (Ref. 26). Table VI presents information for adjusting the analysis for small changes in parameters including  $m^*/m$ .

<sup>26</sup>C. C. Grimes, G. Adams, and P. H. Schmidt, *Bull. Am. Phys. Soc.* **12**, Paper HG6 (1962).

<sup>27</sup>B. Knecht, D. L. Randles, and D. Shoenberg, *Low Temperature Physics-Lt 13, Vol. 4* (Plenum, New York, 1974).

<sup>28</sup>B. Knecht, *J. Low Temp. Phys.* **21**, 619 (1975).

<sup>29</sup>T. M. Rice, *Phys. Rev.* **175**, 858 (1968).

<sup>30</sup>A. H. MacDonald and S. H. Vosko, *J. Low Temp. Phys.* (to be published); S. H. Vosko, J. P. Perdew, and A. H. MacDonald, *Phys. Rev. Lett.* **35**, 1725 (1975).